Data Mine

A High-Resolution Earthquake Catalog for the 2004 M_w 6 Parkfield Earthquake Sequence Using a Matched Filter Technique

Miguel Neves[*1], Zhigang Peng[1], and Guoqing Lin[2]

Abstract

We present the high-resolution Parkfield matched filter relocated earthquake (PKD-MR) catalog for the 2004 M_w 6 Parkfield earthquake sequence in central California. We use high-quality seismic data recorded by the borehole High Resolution Seismic Network combined with matched filter detection and relocations from cross-correlation derived differential travel times. We determine the magnitudes of newly detected events by computing the amplitude ratio between the detections and templates using a principal component fit. The relocated catalog spans from 6 November 2003 to 28 March 2005 and contains 13,914 earthquakes, which is about three times the number of events listed in the Northern California Seismic Network catalog. Our results on the seismicity rate changes before the 2004 mainshock do not show clear precursory signals, although we find an increase in the seismic activity in the creeping section of the San Andreas fault (SAF) (about ∼30 km northwest of the mainshock epicenter) in the weeks prior to the mainshock. We also observe a decrease in the *b*-value parameter in the Gutenberg–Richter relationship in the creeping section in the weeks prior to the mainshock. Our results suggest stress is increasingly released seismically in the creeping section, accompanied by a decreasing aseismic creeping rate before the mainshock occurrence. However, *b*-value and seismicity rates remain stable in the Parkfield section where the 2004 mainshock ruptured. This updated catalog can be used to study the evolution of aftershocks and their relations to afterslip following the 2004 Parkfield mainshock, seismicity before the mainshock, and how external stresses interact with the Parkfield section of the SAF and the 2004 sequence.

Cite this article as Neves, M., Z. Peng, and G. Lin (2022). A High-Resolution Earthquake Catalog for the 2004 M_w 6 Parkfield Earthquake Sequence Using a Matched Filter Technique, *Seismol. Res. Lett.* **XX**, 1–15, doi: 10.1785/0220220206.

Supplemental Material

Introduction

The Parkfield segment of the San Andreas fault (SAF) lies in the transition zone between the mostly seismic southern section and the central creeping section of the SAF (Bakun and Lindh, 1985). With a transitional behavior, deformation in the Parkfield section (Fig. 1) is partially accommodated by repeating M 6 characteristic earthquakes (Bakun and Lindh, 1985). The 28 September 2004 M_w 6.0 Parkfield earthquake was the latest of seven M ∼6 events in this region since 1857 (Bakun *et al.*, 2005; Langbein *et al.*, 2005). From the analysis of the previous six mainshocks until 1966, it was expected that the next rupture would occur no later than 1993 (Bakun and Lindh, 1985). As part of the Parkfield Prediction Experiment (Bakun and Lindh, 1985), a dense network of geophysical instruments, including the 13-station borehole High Resolution Seismic Network (HRSN), were deployed in the area to record in detail the rupture and preparation process of the anticipated mainshock. Thus, the later than expected 2004 M_w 6.0 Parkfield earthquake is one of the best recorded earthquake sequences (Bakun *et al.*, 2005).

The prediction of the future Parkfield mainshock rupture (before 1993) was based on the similarities between the 1934 and 1966 rupture (Bakun and Lindh, 1985; Roeloffs and Langbein, 1994). Whereas both the 1934 and 1966 rupture initiated below Middle Mountain (MM), ruptured unilaterally to the southeast, and were preceded by M 5.1 foreshocks (Bakun and Lindh, 1985), the 2004 mainshock initiated in the southeast of the Parkfield section near Gold Hill (GH) and ruptured mostly to the northwest (Bakun *et al.*, 2005;

1. School of Earth and Atmospheric Sciences, Georgia Institute of Technology, Atlanta, Georgia, U.S.A., https://orcid.org/0000-0002-8581-8551 (MN); https://orcid.org/0000-0002-0019-9860 (ZP); 2. Rosenstiel School of Marine, Atmospheric, and Earth Science, University of Miami, Miami, Florida, U.S.A.

*Corresponding author: mjneves@gatech.edu

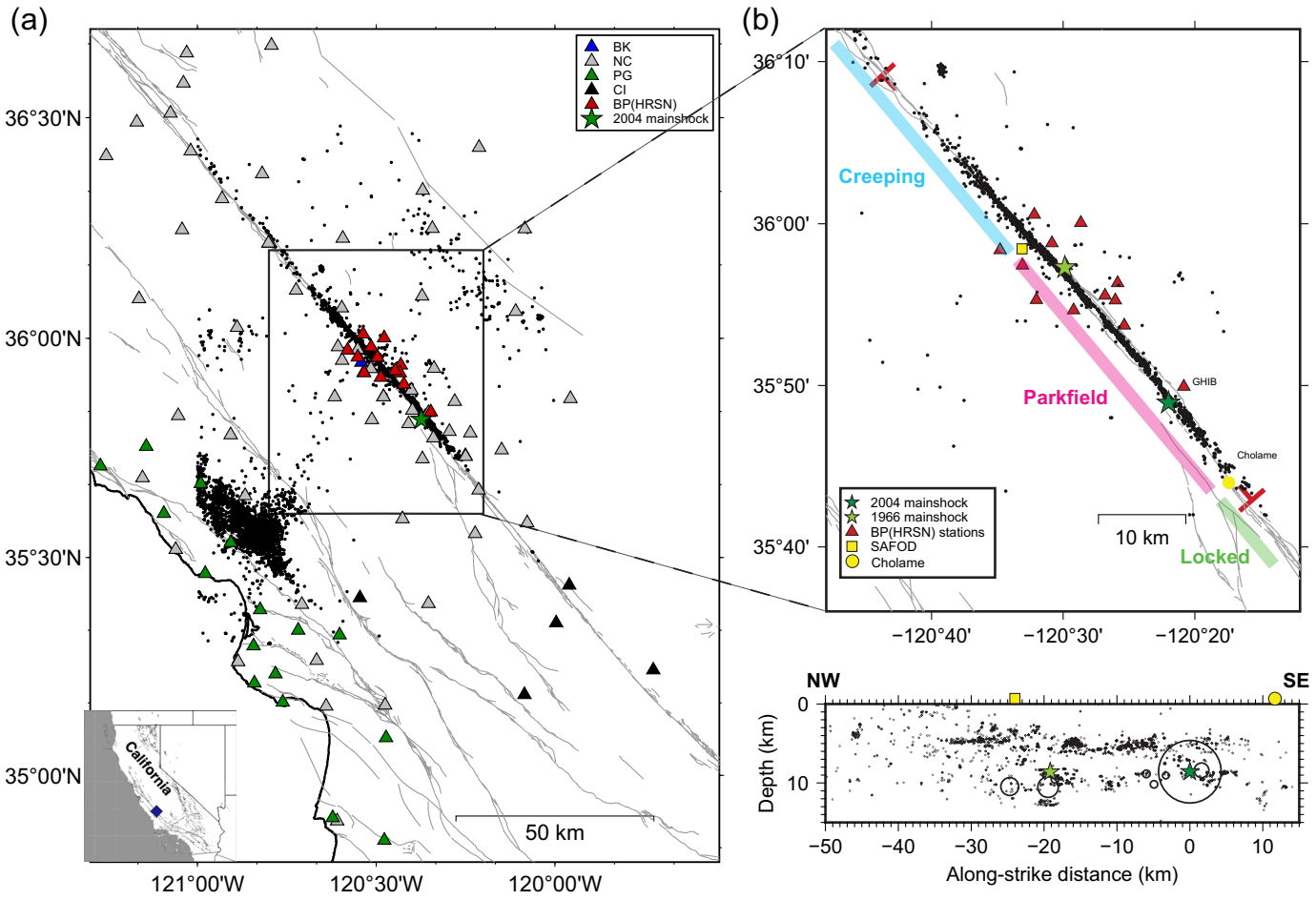

Figure 1. Study area in central California. (a) Map of stations and templates used in our study. Inset shows the location of the study area in California. (b) Location of the local templates. Bottom panel shows an along-strike profile of the earthquakes 5 km away from the San Andreas fault with depth. Different colors denote the fault sections with different slip behaviors, including the creeping, Parkfield, and locked sections, bounded by the San Andreas Fault Observatory at Depth (SAFOD) pilot hole and the town of Cholame. Fault lines in the area are denoted in gray. Red T marks the start and end of the cross section on the bottom panel. The sizes of the earthquakes in the cross-sectional plot scale with their estimated source radius (Peng and Zhao, 2009), which was calculated assuming a circular crack model (Eshelby and Peierls, 1957) and a nominal 3 MPa stress drop using the moment-magnitude relationship by Abercrombie (1996). The color version of this figure is available only in the electronic edition.

Langbein *et al.*, 2005). In addition, no clear precursory signals to the 2004 M 6 earthquake have been identified (Bakun *et al.*, 2005; Langbein *et al.*, 2005; Johnston, 2006), similar to the 1901 and 1922 ruptures for which no foreshocks were reported.

Given the wealth of data available, the Parkfield segment and the 2004 earthquake sequence have been the objects of many seismological studies (Michelini and McEvilly, 1991; Eberhart-Phillips and Michael, 1993; Waldhauser *et al.*, 2004; Peng *et al.*, 2006; Thurber *et al.*, 2006; Custódio and Archuleta, 2007; Nadeau and Guilhem, 2009; Peng and Zhao, 2009; Shelly *et al.*, 2011; Meng *et al.*, 2013; Delorey *et al.*, 2017; Lin, 2018; Perrin *et al.*, 2019; Lin *et al.*, 2022). For example, Thurber *et al.* (2006) derived a 3D compressional wavespeed model using double-difference tomography and relocated more than 20 yr of seismicity at Parkfield, including the 2004 aftershock sequence. Their results show a mostly planar fault at Parkfield, following the southwest fracture zone (SWFZ), rather than the main SAF. Lin (2018) improved earthquake locations using source-specific station term and waveform cross-correlation differential travel-time differences to constrain both absolute and relative locations for earthquakes between 2000 and 2018. Recently, Perrin *et al.* (2019) constrained absolute and relative locations using Thurber *et al.* (2006) 3D model and waveform cross-correlation differential travel-time differences for earthquakes since 1966, and they identified a fault plane being twisted between MM and GH, likely due to the long-term effects of a strong asperity surrounded by a week creeping region. In contrast, Lomax and Savvaidis (2022) apply relocation to earthquakes in the Parkfield segment using source-specific station travel-time corrections combined with waveform coherence and found that their relocated earthquakes follow a single near-vertical fault surface that is planer than observed in previous studies.

However, standard earthquake catalogs are known to be incomplete (Kagan, 2004; Peng *et al.*, 2006; Enescu *et al.*, 2007), especially in the early times after a large mainshock due to the increased noise levels from coda waves of the mainshock and large aftershocks. Peng and Zhao (2009) used a matched filter technique (MFT) to detect additional early aftershocks, and found 11 times more events than those reported in the Northern California Seismic Network (NCSN) catalog in the 3 days following the mainshock. The detailed catalog allowed them to observe an along-strike and down-dip expansion of aftershocks, likely driven by afterslip (Barbot *et al.*, 2009; Jiang *et al.*, 2021). Peng and Zhao (2009) simply assumed the same location of the template events for the detected events. Hence, the resulting locations for the newly detected events were not precise. Also using data from the Parkfield segment, Meng *et al.* (2013) performed a matched filter detection in the month before and after the neighboring M_w 6.5 San Simeon earthquake in 2003 and found that the imposed static stress changes by the 2003 mainshock led to a slight decrease of seismicity in the creeping section, and a slight increase in the seismicity rate around the Parkfield section. This pattern was similar to the changes in low-frequency earthquakes at larger depths in both sections following the San Simeon mainshock (Shelly and Johnson, 2011).

To our knowledge, there is no long-term MFT-detected earthquake catalog in the periods preceding and following the 2004 event with precise relocation and magnitude estimations. Building upon the work of Peng and Zhao (2009) and Meng *et al.* (2013), here we present a high-resolution earthquake catalog from a systematic MFT detection using the recorded HRSN data for the months before and after the 2004 mainshock, which we designate Parkfield matched filter relocated (PKD-MR) earthquake catalog. In the next sections, we describe detailed procedures on how we apply the MFT to detect new events, followed by magnitude calibrations and relocations. We then present initial observations of the aftershock sequence and an analysis of the seismic rate changes and *b*-value variations in the months prior to the mainshock.

Earthquake Catalog Compilation

Matched filter detection

MFT, also called template matching detection, is a detection approach (Gibbons and Ringdal, 2006; Shelly *et al.*, 2007; Peng and Zhao, 2009; Yang *et al.*, 2009; Ross *et al.*, 2019) that allows the detection of earthquakes missed by traditional energy-based detection methods (Allen, 1978). Here, we perform a network-wide MFT detection using the 13 HRSN stations (Fig. 1) following a similar procedure to Meng *et al.* (2013). The detection period is from 6 November 2003, 46 days before the neighboring M_w 6.5 San Simeon earthquake (same starting date in Meng *et al.*, 2013 study), to 28 March 2005, 6 months after the 2004 M 6 Parkfield mainshock. The BP channel data (20 samples/s) were used. We first apply a 2–8 Hz two-way fourth-order band-pass filter to the seismic data. To compile our template catalog, we use two relocated catalogs for northern California. We use Lin (2018) catalog for Parkfield, which includes earthquakes along the SAF as our main template catalog. To include events located off the main SAF and templates from neighboring regions such as the San Simeon aftershock zone, we add earthquakes in the NCSN relocated catalog (Waldhauser and Schaff, 2008) with the Caltech–USGS Seismic Processing event ids not included in Lin (2018) (Fig. 1a). We select cataloged earthquakes between latitude 35.3° and 36.4° N and longitude 120.0° and 121.0° W. We consider earthquakes located less than 20 km away from the SAF as local templates (Fig. 1b).

We retrieve available *P*- and *S*-phase arrival times from the Northern California Earthquake Data Center for the templates or attempt to pick arrivals with PSIRPicker (Li and Peng, 2016) for events and stations with no reported arrivals. The PSIRPicker uses a general 1D velocity model (Table S1, available in the supplemental material to this article) to predict the initial *P* or *S* arrivals, followed by a simple short-term average/long-term average detector (Allen, 1978) to pick the accurate arrivals. The majority of our *S*-phase picks (99%) are from the PSIRPicker results because only six *S*-phase picks could be retrieved from the NCSN catalog for the HRSN stations. We then compute the signal-to-noise ratios (SNRs) for each event at each channel (*P* phases on vertical channels and *S* phases in the horizontal channels) by comparing the sum of squared amplitudes in a 5 s window before the phase arrival with a 5 s window after the arrival. Only earthquakes with at least SNR > 5 arrivals at 12 channels were included in the template catalog. This results in a catalog with a total of 10,184 template earthquakes between 6 November 2003 and 28 March 2005 (Fig. 1a).

Detection was performed using waveforms from −1 to 4 s around the *P*-phase arrival in the vertical channels and around the *S*-phase arrival in the horizontal channels. Using only channels with SNR > 5, we cross-correlate each template waveform at each channel with the corresponding channel's daily waveform (86,460 s long). We then shift daily cross-correlation functions (CCFs) for each channel to the origin time of the correlating template and stack to obtain a network averaged daily CCF. Peaks above 12 times the median absolute deviation value of the averaged CCF (Fig. S1) were selected as detections (Ross *et al.*, 2019; Zhai *et al.*, 2021). Because one event can be detected by more than one template, we look for detections with overlapping windows in any of the channels used for detection. In these cases, we keep only the detection of the template with the highest cross-correlation coefficient (CCC) as in Meng *et al.* (2013) (i.e., the best detecting template). The newly detected events are initially assigned the hypocentral location of the best detecting template.

For the periods of 13 and 14 May 2004, 29 December 2004 to 12 January 2005, and 20–22 February 2005, the majority of the HRSN network stations do not have complete daily records. In these periods, we perform detections using the channels with complete 24 hr waveforms and include seismic

stations from the NC network in a 0.5° radius area from the 2004 mainshock location.

We include templates distanced up to about 50 km from the region of interest to remove false detections of distant events as local detections, for example, from the M_w 6.5 San Simeon earthquake area (e.g., Meng *et al.*, 2013). The use of separate template *P* and *S* window allows detection of events with slight variations in *S*–*P* times, but it is also prone to false detections from local templates that correlate strongly with impulsive *P* or *S* arrivals of distant large earthquakes, contaminating our detection catalog. Using distant events as templates, we can identify these false detections by removing events for which the best detecting template is located more than 20 km away of the SAF.

This results in a total of 115,263 detections with 28,107 events being best associated with local templates. These 28,107 detections formed our local detection catalog (Data set S1), which was used for subsequent relocation. In comparison, 4393 events are listed in our template catalog in the same space–time windows (Data set S2).

Earthquake relocation

We constrain the relative locations of the new detections in our catalog using cross-correlation derived differential travel times (e.g., Waldhauser, 2000; Waldhauser and Schaff, 2008; Lin, 2018). We use the XCORLOC package (Lin, 2018) to perform differential travel-time relocation. The first step in our relocation process was to improve the azimuthal coverage. We retrieve all waveforms from stations in all available seismic networks in the region (Fig. 1a). These include mostly stations from the NCSN (network code NC) but also from the Southern California Seismic Network (network code CI), the Central Coast Seismic Network (network code PG), as well as the HRSN (network code BP) that were used in the initial MFT detection.

As mentioned before, we assume that the newly detected events have the same initial hypocenter as the best detecting template and assign the corresponding phase arrival times to the new detections. To calculate differential travel times, we cross-correlate each event with all possible pairs in a 5 km radius. We use −0.5 to 1.5 s around the *P*-phase arrival for the vertical channels, truncating if *S* phase is included in the window (Shelly *et al.*, 2013), and −0.5 to 2.0 s around the *S*-phase arrival for the horizontal channels. In the case of the *S* phase, we keep the measurement of the horizontal channel with the highest CCC. To ensure millisecond precision we retrieve the waveforms from available channels with the highest sampling rate (e.g., the DP channel for HRSN with 250 samples/s) and use a spline interpolation technique to 1 ms in the samples around peak cross correlation. Similar to the detection stage, cross correlation is performed using 2–8 Hz band-pass filtered data. We use only differential times when the measured CCCs are greater than 0.7. Each event pair must have at least eight differential travel time measurements and an event needs to pair with at least one template to be considered for relocation. We then input the resulting differential travel times into XCORLOC using the velocity model for Parkfield as reported in the NCSN catalog (Oppenheimer *et al.*, 1993). We perform relocation by keeping template events location fixed. We estimate uncertainties as in Lin (2020) with a bootstrap method by repeating 15 times (Figs. S2 and S3). Our final catalog (PKD-MR catalog, Data set S3) includes 13,914 earthquakes (Fig. 2) about 3.2 times the number of earthquakes in our local templates catalog.

Magnitude calibration

To estimate the magnitudes of the events in our new catalog, we follow a similar procedure to previous matched filter studies (Peng and Zhao, 2009; Meng *et al.*, 2013; Shelly *et al.*, 2016; Shelly, 2020; Yao *et al.*, 2021). We estimate the magnitude of the new events (M_{New}) by comparing its amplitude with the template magnitude ($M_{Template}$) and amplitude:

$$M_{New} = M_{Template} + c \times \log_{10} a, \quad (1)$$

in which *a* corresponds to the amplitude ratio between the newly detected events and the detecting template and *c* to a calibration factor. Different approaches have been used to determine *a*, such as peak amplitudes ratio (Peng and Zhao, 2009), least-squares fit (Gibbons and Ringdal, 2006), or principal component fit (Shelly *et al.*, 2016). Peak amplitude ratio considers only one data point and can be easily affected by noise. To estimate the magnitude of the newly detected events, we follow a similar method proposed by Shelly *et al.* (2016) and Shelly and Hardebeck (2019) to extend the duration magnitude M_d scaling of the templates catalog to the newly detected events by a principal component fit.

Specifically, we calibrate magnitudes for the same pairs used in the relocation procedure. That is, we compare the signals of the newly detected events with each template that pairs with at least 8 CCCs above 0.7. The amplitude ratio for each measurement is then calculated using a principal component fit using the −0.5 to 1.5 s time window for the vertical channels and −0.5 to 2 s for the horizontal channels. The amplitude ratio for each pair corresponds to the median of the amplitude ratio measurements at each channel. To avoid biases resulting from comparing different magnitude types, we limit our estimates using only templates with reported M_d. To estimate the calibration factor, we compare the amplitude ratios of the templates and their cataloged magnitude differences (Shelly *et al.*, 2016). We obtain a value of 0.828 for *c* (Fig. S4). The final magnitude estimate for a new detection corresponds to the median of the magnitude estimates obtained from each detection-template pair (Fig. 2c).

General Properties of the New Catalog and Potential Limitations

The PKD-MR earthquake catalog has 13,914 earthquakes (Fig. 2). The first aftershock listed in our relocated catalog

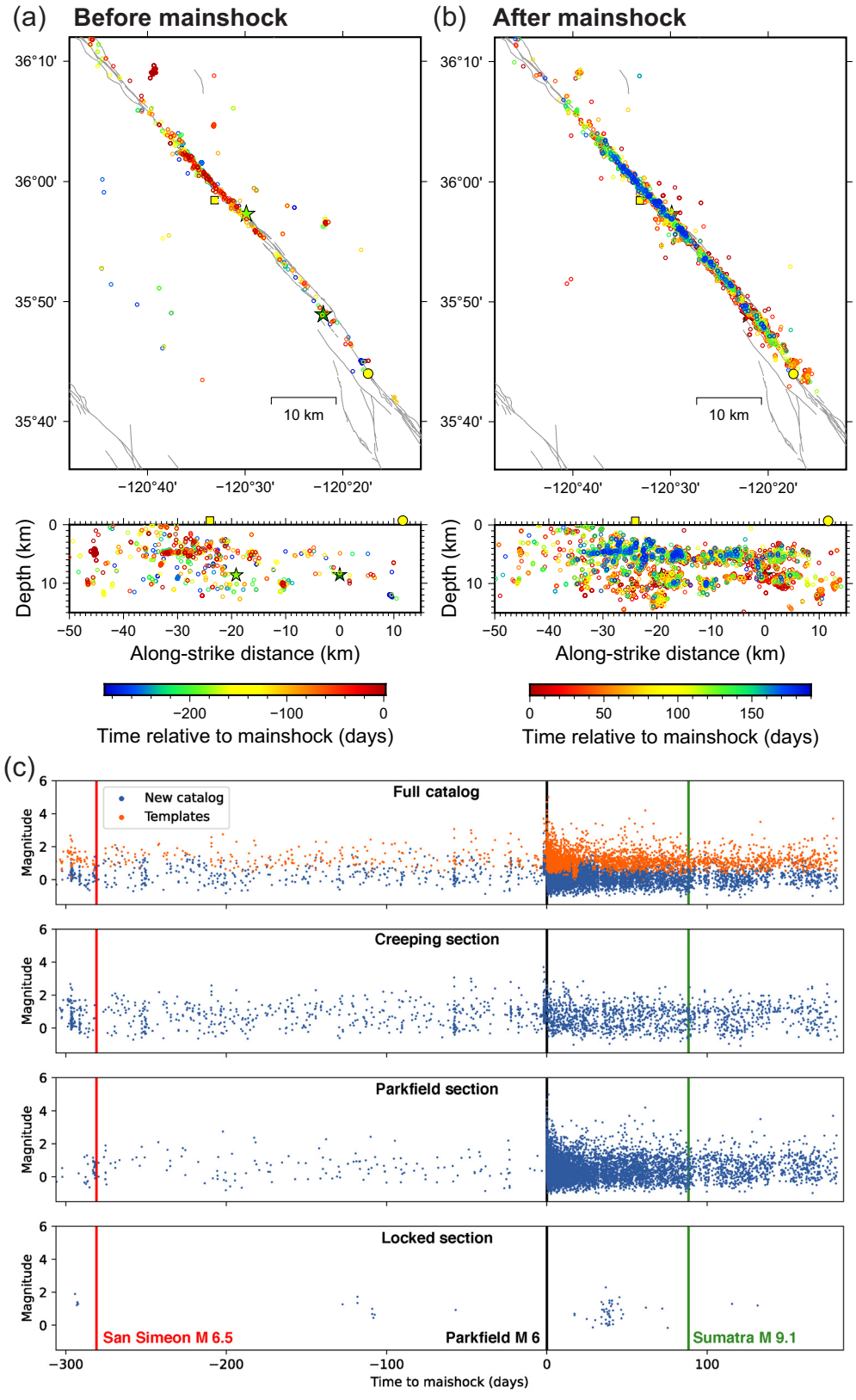

Figure 2. General pattern of the newly relocated earthquake catalog. (a) Plot of the earthquakes in the new catalog in the period before the mainshock, with color denoting time relative to mainshock. (b) The same as panel (a) but showing aftershocks. In both plots, red colors indicate events happening closer to the mainshock. (c) Plot of earthquake magnitudes with time for the entire Parkfield segment and each of the fault sections. Vertical lines mark the times of three major earthquakes during the study period. The color version of this figure is available only in the electronic edition.

was detected 99 s after the mainshock located about 15.8 km northwest of the mainshock epicenter, with a magnitude of 2.46 (Fig. 3). Matched filter detection in our chosen frequency band (2–8 Hz) fails to detect early aftershocks in the first minutes after the mainshock due to its high coda wave energy (Fig. S5). Still, this is a significant improvement to the NCSN catalog, in which the first cataloged aftershock is detected 222 s after the mainshock.

As seen in previous studies, large magnitude earthquakes correlate poorly with small- and moderate-size earthquakes (e.g., Lin, 2020; Shelly, 2020). Hence, large earthquakes in our catalog such as the M 6 mainshock and the two largest M 5 aftershocks are not relocated. For these earthquakes, we add the locations listed at Lin (2018) catalog to the new catalog. Therefore, caution should be taken when comparing the locations of the larger earthquakes with the relative locations of the other events.

We show a comparison of the PKD-MR catalog with the catalogs from Lin (2018), Thurber *et al.* (2006), and Waldhauser and Schaff (2008) in Figure 4 (see also Movie S1). Locations of earthquakes in the new catalog are similar to the previously relocated catalogs in the region delineating the same seismic structures but with additional events (Fig. 4). Here, we observe that most events are located below the SWFZ, and shallow events form a flower-type structure, which were also reported before by Thurber *et al.* (2006) (Fig. 4b). Depths in the new catalog are in-line with those observed in Lin (2018) catalog

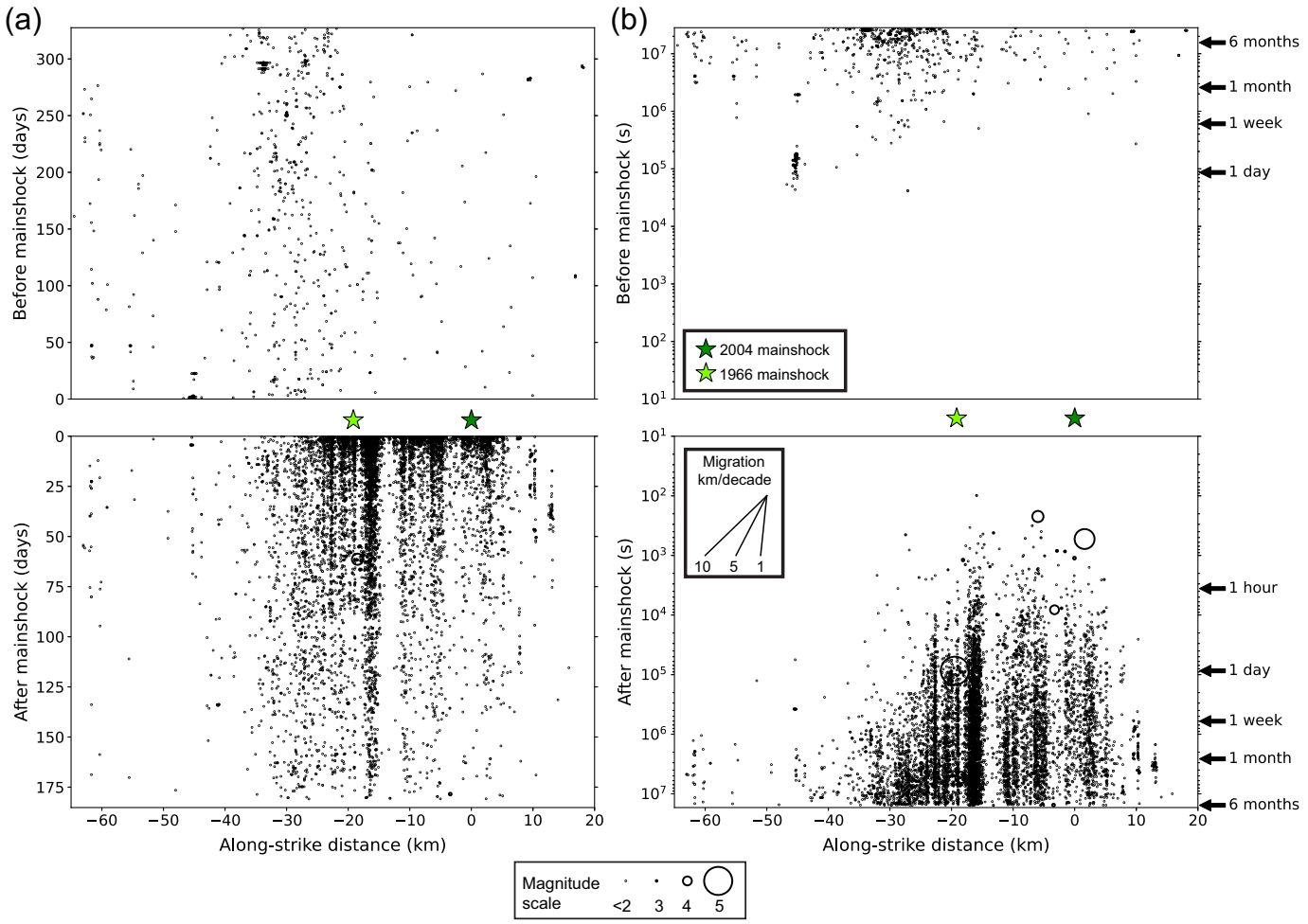

Figure 3. Along-strike distribution of the events in our relocated catalog with time. (a) Occurrence time of events in days with a linear time scale. (b) Occurrence time of events in seconds with a logarithmic time scale. The color version of this figure is available only in the electronic edition.

that we use to build our local template catalog with average depth decreasing 14 m after relocation (Fig. S6). When comparing with Thurber *et al.* (2006) and Waldhauser and Schaff (2008), we observe slight variations in depth, in particular the deepest cluster at about 20 km northwest of the mainshock epicenter along-strike extends between 12 and 13 km in our new catalog and Lin (2018) catalog. In comparison, events in Thurber *et al.* (2006) extend from about 12.5–14 km and even deeper depths between 13.5 and 14.5 km in Waldhauser and Schaff (2008) catalog (Fig. 4c), which are likely due to the different velocity models used in the relocation process.

The PKD-MR catalog includes 10,280 events for which we were able to estimate the magnitude. The remaining 3634 events in the catalog have no estimated magnitude because they correspond to templates with no magnitude reported at the NCSN catalog or detections that correlate only with these templates. We allow template magnitudes to change when they correlate with other templates. We observe on average a −0.04 change in the template magnitudes (Fig. S7); therefore, magnitudes can be different from those reported in the NCSN and other relocated catalogs.

It is widely observed that earthquake magnitudes follow the power-law distribution, also known as the Gutenberg–Richter (GR) relationship (Ishimoto and Iida, 1939; Gutenberg and Richter, 1944) in the form of

$$\log(N) = a - bM, \tag{2}$$

in which N corresponds to the cumulative number of earthquakes with a magnitude equal to and larger than M. a and b are constants, in which a corresponds to the expected number of earthquakes with magnitudes larger than or equal to 0, and b indicates the relative number of larger magnitude earthquakes versus smaller magnitude earthquakes in the distribution (i.e., the b-value).

As mentioned before, earthquake catalogs are inherently incomplete due to, for example, limitation in seismometer sensitivity, station coverage, or overlapping arrival of seismic waves (Kagan, 2004; Peng *et al.*, 2006; Enescu *et al.*, 2007; Peng and Zhao, 2009). Hence, a magnitude threshold is usually

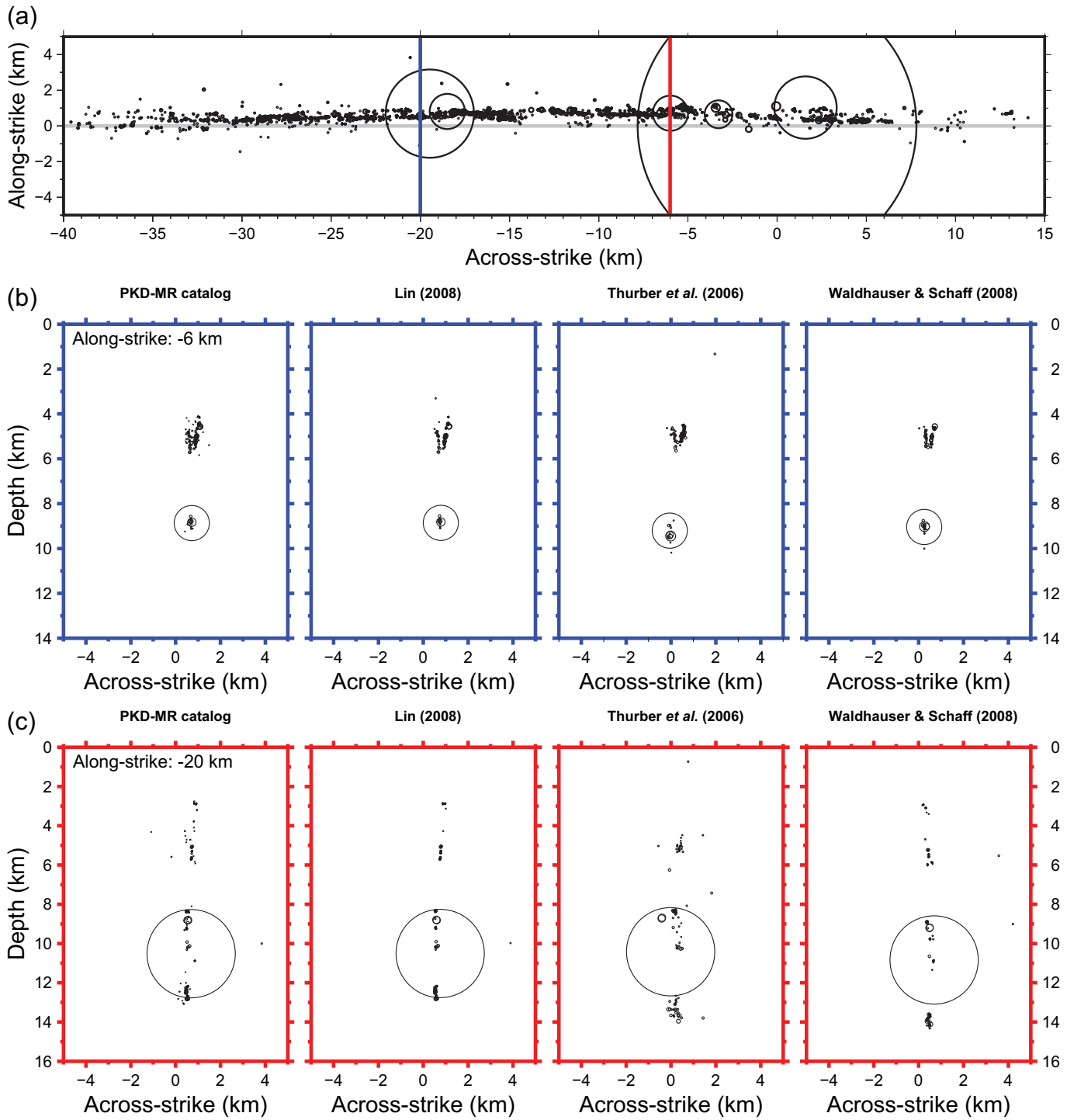

defined, above which the magnitudes follow the GR distribution, and the catalog is assumed to be complete. Such threshold is called magnitude of completeness (M_c). M_c has been shown to vary significantly spatially and with time (e.g., Wiemer and Wyss, 2000; Kagan, 2004) and depends on variables such as number of samples or the estimation method (Woessner and Wiemer, 2005). The choice of M_c can have a significant impact on the statistical properties derived from the catalog (e.g., Woessner and Wiemer, 2005; Herrmann and Marzocchi, 2021; van der Elst, 2021). We estimate the new completeness

Figure 4. Comparison of our catalog with different relocated catalogs for Parkfield. (a) Earthquakes in the new Parkfield matched filter relocated (PKD-MR) earthquake catalog above estimated apparent magnitude of completeness (AM_C) (0.6). Red and blue lines mark locations of 2 km cross sections shown in panels (b) and (c), respectively. The gray line marks the zero cross-fault distance. The sizes of the earthquakes scale with their estimated source radius following the same method as Figure 1. Movie S1 shows cross sections along the entire study area. The color version of this figure is available only in the electronic edition.

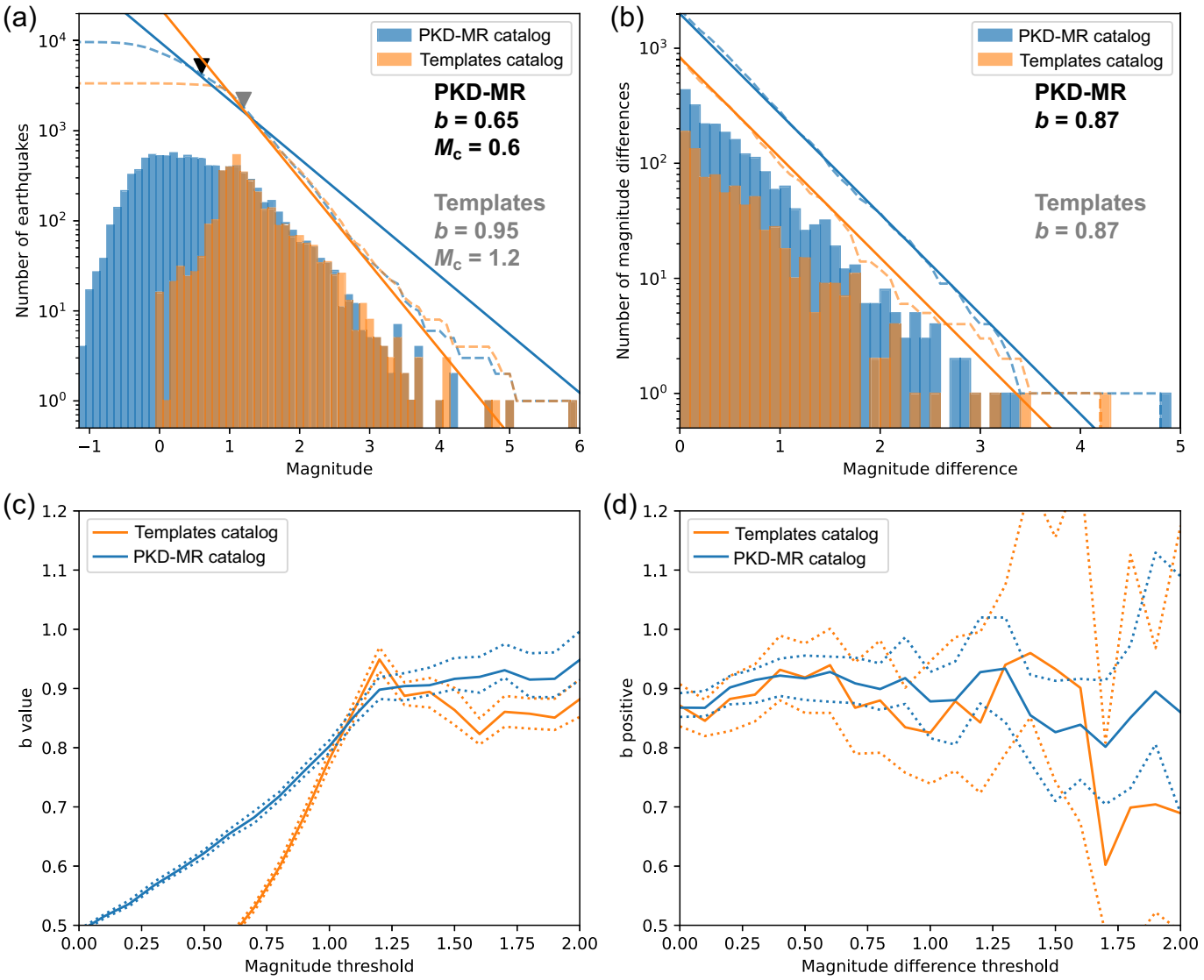

Figure 5. (a) Gutenberg–Richter distribution of the template catalog (orange) and the new relocated catalog (blue). *b*-value maximum likelihood and AM_C estimates are denoted in gray and black for the template and the new catalog, respectively. (b) Distribution of positive magnitude differences above AM_C. *b*-positive maximum-likelihood estimates are denoted in gray and black for the template and the new catalog, respectively. (c) Variation of *b*-value estimates with assumed magnitude of completeness. Uncertainties are estimated by bootstrapping. (d) Variation of *b*-positive estimates with assumed minimum magnitude difference. The color version of this figure is available only in the electronic edition.

following the entire magnitude range (EMR) method of Woessner and Wiemer (2005), which considers the entire data with a two-part model, a power-law model above M_c, and a normal cumulative distribution below M_c.

Binning the catalog in 0.1 magnitude intervals, we estimate M_c of 0.6 for the new catalog (Fig. 5a), an apparent improvement to the template catalog for which we estimate a completeness of 1.2. Caution is necessary when interpreting the M_c parameter for the PKD-MR catalog (Herrmann and Marzocchi, 2021). We observe a clear change in the GR distribution trend above and below magnitude 1.2 (Fig. 5a). This is also reflected in our *b*-value estimates. Using the maximum-likelihood estimator, we obtain a *b*-value of 0.65 for the new catalog and of 0.95 for the template catalog (Fig. 5a). This is because the new catalog is not actually complete below 1.2 due to the limitations of the MFT method (e.g., improper mixing of different magnitude scales, spatiotemporal varying incompleteness; Herrmann and Marzocchi, 2021). In addition, MFT only detects events similar to the templates within certain distance ranges, and with our detection parameters, we do not allow detection of events with significant overlaps. Finally, even though the MFT is more robust than traditional detection methods, variations in background noise levels still impact its detection performance. We therefore use apparent magnitude of completeness (AM_C) to refer to estimates using the PKD-MR catalog. As expected, M_c estimates vary with time and the same occurs with AM_C

estimates with larger AM_C in the period right after the mainshock, when noise levels are higher due to the mainshock coda waves, and during the periods when several of the HRSN stations were down. In these later periods, our AM_C estimates do not show significant improvements, even though we use the NC stations to perform additional detections.

Recently, van der Elst (2021) proposed a new *b*-value estimator insensitive to variations of catalog completeness with time. This *b*-positive estimator (b^+) calculates *b*-value considering positive magnitude differences ($\overline{m'}$) of consecutive earthquakes above a minimum magnitude difference (M_c'):

$$b^+ = [\ln(10)(\overline{m'} - M_c')]^{-1}, \overline{m'} \geq M_c'. \quad (3)$$

We use the *b*-positive estimator with the magnitude of completeness correction, considering only earthquakes with magnitudes above our estimated AM_C. Using this method we estimate a *b*-value of 0.87 for both the template and PKD-MR catalogs (Fig. 5b). These values are more in line with previous *b*-value estimates of 0.92 at Parkfield (Schorlemmer *et al.*, 2004) and are stable with different choices of the minimum magnitude difference (Fig. 5d). This result can be explained with the same argument that van der Elst (2021) proposed for the use of the positive magnitude differences. The occurrence of a larger earthquake limits the detection capability of a subsequent smaller earthquake, which also applies in the MFT detection. We therefore suggest the use of the *b*-positive estimator for statistical analysis with our PKD-MR catalog (and other catalog built with MFT) and caution with the magnitude of completeness parameters.

Aftershock Expansion

We present here a general description of the earthquake sequence using the PKD-MR catalog. Peng and Zhao (2009) previously analyzed the early aftershock sequence using a MFT improved catalog for the first three days after the mainshock, but their analysis did not include relocation of the new detections. In their study, Peng and Zhao (2009) observed a linear migration of early aftershocks with logarithmic-time along-strike and down-dip, and they interpreted as an expansion driven by afterslip (Kato, 2007).

Here, we extend the observation of aftershocks to 6 months after the mainshock. As expected, we also observe a migration with logarithmic time along-strike of the early aftershocks (Fig. 3b). A similar expansion is observed in terms of depth (Fig. S8). Along-strike, this expansion is larger to the northwest (toward the creeping section) and more limited toward the southeast (toward the locked section). The logarithmic-time expansion to the northwest extends to about 38 km of the mainshock epicenter during the first 14 days (Fig. 3). Further than this point, seismic activity in the creeping section appears to resume during the first week after the mainshock with rates similar to those observed before the mainshock (Fig. S9).

In terms of depth (Fig. S8), the first detected aftershock is located at 5 km depth, and after this aftershock a linear expansion with logarithmic time is observed both in the down-dip direction and up-dip direction. This depth logarithmic-time expansion occurs during the first week after the mainshock.

Precursory Activity

Seismic or aseismic activity in the period leading to large mainshocks has been the object of several studies for decades (Roeloffs, 2006; Pritchard *et al.*, 2020; Kato and Ben-Zion, 2021; and references therein) with the goal of understanding the nucleation process and identifying possible warning signals of the impending earthquake. Precursory signals and earthquake initiation is usually explained in the framework of two models): the cascade model, which explains mainshock triggering as a result of stress perturbations imposed by a sequence of preceding earthquakes, also known as foreshocks (Olson and Allen, 2005; Mignan, 2014); the pre-slip model that considers rupture initiates due to an aseismic process such as slow-slip that leads to the rupture of surrounding asperities (Dieterich, 1978; Mignan, 2014). Other proposed frameworks for precursory activity include progressive localization (Ben-Zion and Zaliapin, 2020), in which deformation along a distributed region progressively concentrates to primary slip zones culminating in large earthquakes, and seismic quiescence (Mogi, 1969; Wyss and Habermann, 1988), when a significant decrease in seismicity is observed prior to a mainshock.

Precursory activity is still an open question in the Parkfield earthquakes. Although previous mainshocks were preceded by moderate foreshocks, no foreshocks have been found in the 2004 mainshock (Bakun *et al.*, 2005). Nonetheless, possible evidence of precursory signals has been identified retrospectively (Nadeau and Guilhem, 2009; Chun *et al.*, 2010; Shelly and Hardebeck, 2019). For example, Nadeau and Guilhem (2009) identified an unusual deep tremor episode three weeks before the 2004 mainshock, based on the envelope function of the HRSN recordings. Using low-frequency earthquakes as templates, Shelly (2009, 2017) found elevated tremor rates and southward tremor migration in the 3 months before the 2004 Parkfield mainshock. However, most tremor events occurred in Cholame, which is at least 20 km away from the initiation point of the Parkfield mainshock. Chun *et al.* (2010) observed a rise in *P*-wave attenuation 18 months before the mainshock. However, based on cross correlation of ambient seismic noises, no clear change in seismic velocity was observed before the mainshock, except an abrupt velocity reduction caused by the nearby 2003 M_w 6.5 San Simeon earthquake (Brenguier *et al.*, 2008; Zhao *et al.*, 2010). Ben-Zion and Zaliapin (2020) examined the localization processes of earthquakes in the Parkfield segment and observed a delocalization prior to the 2004 mainshock, which they suggested can be the result of increasing stress around the Parkfield asperity.

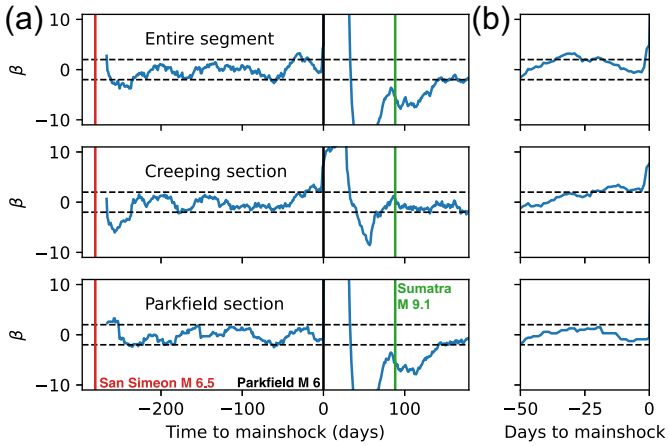

Figure 6. Variation of β-statistics at the studied period using two 30-day moving windows and our new PKD-MR catalog. (a) Three panels show variations considering the entire Parkfield segment and the different sections of the fault. (b) Detailed view of the 50 days prior to the mainshock. The color version of this figure is available only in the electronic edition.

Using the PKD-MR catalog, we identify no clear signal of precursory micro earthquake activity (Fig. 2). No migration pattern either toward or away from the epicenter is identified (Figs. 2a and 3). We use β-statistics to identify significant seismicity rate changes with time (Matthews and Reasenberg, 1988; Aron and Hardebeck, 2009). β-statistics compares the number of observed earthquakes in a period to the number of expected earthquakes in that period based on the observations of a background period. We estimate β using two adjacent moving time windows of 30 days (Fig. 6) moving forward by one day and consider a significant rate change when $|\beta| > 2$. Each measurement corresponds to the last point in the window, meaning only earthquakes before the measurement are considered. We consider only events distanced less than 5 km off the SAF for this analysis. Results are similar when considering different magnitude and distance thresholds and time windows (Figs. S10–S14). In addition, we estimate the coefficient of variation of the interevent times and the ratio of maximum seismic moment to total seismic moment following a method similar to Cabrera *et al.* (2022). These parameters give information on the temporal clustering of seismicity and how moment is released during the seismic sequence, respectively (Figs. S15 and S16). We use a 150-event moving window that moves forward by one event including events above AM_C.

For the entire Parkfield segment (Fig. 1b), we observe two periods that show significant changes that appear to be related to seismic activity at the creeping section (Fig. 6). Following the neighboring M_w 6.5 San Simeon earthquake, there is a significant decrease in β in the creeping section and a significant increase in the Parkfield section similar to the observations by Meng *et al.* (2013). Prior to the Parkfield M_w 6 mainshock, we observe a steady increase of the seismicity rate in the creeping section starting 49 days before the mainshock that becomes significant 17 days prior to the mainshock. In the 48 hr before the mainshock we identify a jump in β estimates to 7.1, suggesting a sudden increase of activity in the creeping section prior to the mainshock. The β increase in the days before the mainshock coincides with the peak of ratio of maximum seismic moment to total seismic moment in the creeping section (Fig. S15). However, no significant changes are observed in the Parkfield section where the mainshock ruptured in the same period (Figs. 3 and 6; Figs. S15 and S17). We also observe no significant variations in the temporal clustering of events, which shows a gradual decrease in the clustering of events following the occurrence of the neighboring M_w 6.5 San Simeon earthquake (Fig. S16).

Temporal Variations of *b*-Value

We also analyze the temporal variations of the *b*-value parameter of the GR distribution (Fig. 7). The actual significance of the *b*-value in the GR distribution is still debated (e.g., Marzocchi *et al.*, 2019), but recent studies observe that the *b*-value is inversely related to differential stress both on laboratory settings (Amitrano, 2003) and field (e.g., Schorlemmer and Wiemer, 2005; Scholz, 2015). Tormann *et al.* (2013) analyzed the variations of *b*-values at Parkfield and connected it to surface creep rate variations with decreasing *b*-values correlating with decreasing creep and increasing loading stresses on the fault. More recently, Gulia and Wiemer (2019) studied 58 aftershock sequences and observed that the *b*-value can be an indicator if a large earthquake is the mainshock or a foreshock. Nanjo (2020) also observed that for the 2019 Ridgecrest earthquake sequence the locations of the larger M 6.4 foreshock and the M 7.1 mainshock could be retrospectively identified by analyzing *b*-values in the area.

To estimate the time variations of *b*-value, we consider the methodology and findings of previous studies that perform similar time variation analysis such as Gulia and Wiemer (2019), Dascher-Cousineau *et al.* (2020), and van der Elst (2021). We also consider the findings by Marzocchi *et al.* (2019) on the best practices to estimate *b*-values. We analyze all events in the PKD-MR catalog with estimated magnitudes and distances less than 5 km of the SAF strike. We also test different distance values between 2 and 10 km (Figs. S18 and S19). We define a moving window of 150 events that moves forward by one event. We then estimate the AM_C for the window using the EMR method. For event windows with at least 50 events above AM_C, we estimate the *b*-value using the *b*-positive estimator (van der Elst, 2021). A *b*-positive estimate is deemed robust if the distributions had more than three magnitude bins with events and passes a Lilliefors test (a = 0.05) to ensure exponentiality of the magnitude differences distribution (Lilliefors, 1969; Marzocchi *et al.*, 2019). We further identify periods of significant *b*-positive variations

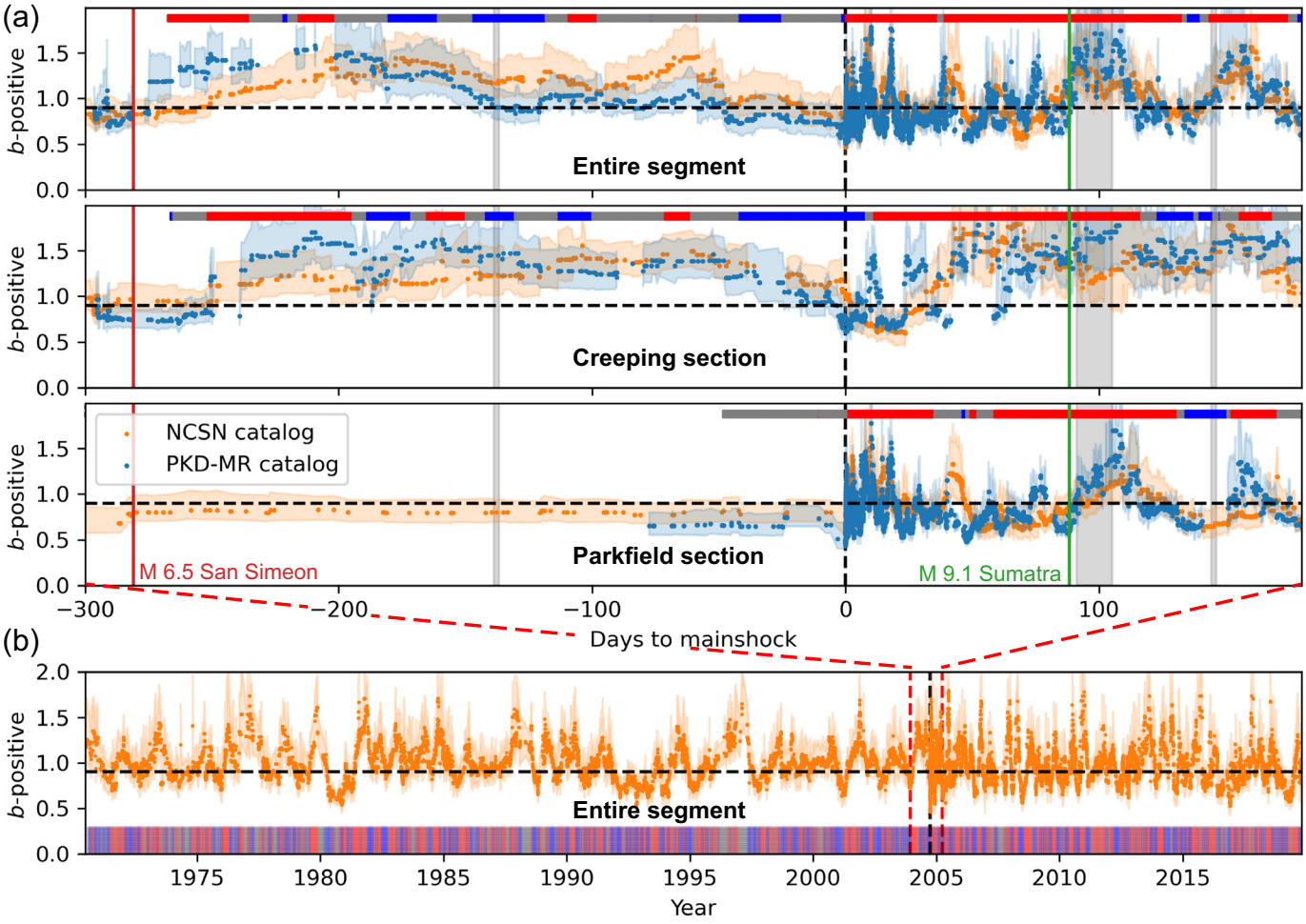

analyzing the slope of a fitted linear function using 30-day length time windows (see the supplemental material).

Variations of the *b*-positive parameter are commonly observed at Parkfield since 1970. *b*-positive varies between a minimum of 0.47 recorded 20 min after the 2004 mainshock and a maximum of 1.79 recorded 10 months after. Other particularly low *b*-positive estimates of 0.52 are also recorded in 1992 with the occurrence of M > 4 earthquakes (Roeloffs and Langbein, 1994). Estimates of *b*-positive using the PKD-MR catalog show in general similar trends to estimates obtained using the NCSN catalog (Fig. 7) but with shorter period variations, because a smaller time window is used for the PKD-MR catalog. In the aftershock period PKD-MR catalog estimates show higher variability but the long-term trends are consistent with the NCSN catalog. Using the PKD-MR catalog we can get a more detailed picture of the *b*-positive temporal variations.

Estimates of *b*-positive in the Parkfield section are generally stable prior to the 2004 mainshock considering both catalogs (Fig. 7), suggesting variations in the entire segment (Fig. 1) prior to the mainshock are driven by the creeping section. After the nearby M_w 6.5 San Simeon earthquake, we identify an increase in *b*-positive in the creeping section peaking at 1.71, 80 days after the San Simeon earthquake. After this peak, estimates show some variability with periods of decrease and increase until about 47 days prior to the 2004 mainshock when we start to observe a period of significant decrease. This decreasing period lasts through the first week after the 2004 mainshock and *b*-positive estimates drop from 1.4 to 0.6.

In contrast, after the mainshock, *b*-positive variations in the entire segment resemble the *b*-positive variations in the Parkfield section suggesting *b*-positive is driven by seismicity in the Parkfield section during this period. Though strong

Figure 7. Time variations of *b*-value using the *b*-positive estimator. (a) Shows variations for the Parkfield segment and the creeping and Parkfield sections. Gray-shaded areas indicate periods in which most High Resolution Seismic Network stations do not have complete daily records. (b) Shows estimates for the entire Northern California Seismic Network catalog. Color bars at the top in (a) and bottom in (b) show identified periods of significant *b*-positive changes using our slope analysis, in which red corresponds to significant increases, blue to significant decreases, and gray to no significant changes. The color version of this figure is available only in the electronic edition.

oscillations are observed, there is a general trend of increasing *b*-positive in the entire area consistent with the increased occurrence of the smaller aftershocks. Following the occurrence time of the 2004 M_w 9.1 Sumatra earthquake, there is a *b*-positive peak, also observed in the NCSN catalog. However, this peak appears to initiate before the Sumatra earthquake, similar to a variation observed in the β-statistics (Fig. 6), and this period also coincides with the HRSN network outage. Additional analysis is necessary to clarify what drives this variation and if there is a relation to the M_w 9.1 Sumatra earthquake, which has been observed to impact tremor rates in Parkfield (Ghosh *et al.*, 2009).

Discussion

Using the high-quality data of the HRSN network and matched filter detection, we compiled a high-resolution catalog for the Parkfield segment of the SAF spanning from 6 November 2003 to 28 March 2005, including the 2004 M_w 6 mainshock. Events in the PKD-MR catalog have high-precision relative locations (see the supplemental material) obtained by cross-correlation derived differential travel times and magnitude estimations based relative amplitude measurements.

Our initial analysis of the temporal evolution of earthquakes in the months before the 2004 M_w 6 earthquake does not indicate clear precursory signals near the mainshock epicenter. However, we find significant changes in the creeping section. β-statistics show a significant seismic activity increase about 49 days before the mainshock (Fig. 6) around the same time a significant *b*-positive decrease is identified (Fig. 7). A more pronounced β increase is also observed in the 48 hr before the mainshock that coincides with an increased seismic moment release in the creeping section. A decrease of the seismic rate in the creeping section after the stress changes imposed by the neighboring M_w 6.5 San Simeon earthquake (Meng *et al.*, 2013) also relate to positive variations of *b*-positive. These results are consistent with the observations of Tormann *et al.* (2013) and Khoshmanesh and Shirzaei (2018) that connected *b*-value variations at Parkfield with creeping rates. However, this does not explain all the smaller *b*-positive variations observed in the aftershock period as they do not relate to the observed seismicity rates. Regardless, our observations suggest an increased release of stress seismically with an increase in the number of earthquakes with larger magnitudes and a decrease in the aseismic creeping rate in the creeping section prior to the 2004 mainshock. In the same period, seismic activity remains stable in the rupturing Parkfield section. Because these changes are observed in the creeping section with a median along-strike distance of more than 30 km northwest of the mainshock epicenter (Fig. 3; Fig. S17), we are unable to connect them to the mainshock nucleation process. These changes in the creeping section could be related to a larger scale preparation process like the aforementioned delocalization prior to the 2004 Parkfield mainshock (Ben-Zion and Zaliapin, 2020) or the slow slip event (SSE) identified in the Parkfield area by Khoshmanesh and Shirzaei (2018). Still, the analysis of Ben-Zion and Zaliapin (2020) shows delocalization more than a year prior to the mainshock, and changes we observe occur only weeks before. Khoshmanesh and Shirzaei (2018) identified that SSE starts in the creeping section in 2003 and appears to migrate toward the Parkfield section with a rate decrease in the area where we identify the seismic changes. This SSE observation can explain the seismic rate increase and *b*-positive decrease that we observe in the creeping section. But it is still intriguing why no seismic changes are identified in the Parkfield section due to the SSE. We also observe that no other precursory changes have been observed in the Parkfield section before the mainshock like strain measurements (Borcherdt *et al.*, 2006; Johnston *et al.*, 2006). These observations add to a number of other changes observed prior to the 2004 mainshock also without a clear connection to the mainshock rupture (e.g., Bakun *et al.*, 2005).

The mechanisms of the Parkfield sequence still have many unanswered questions that the wealth of data in our new catalog could potentially address. Especially in the early aftershock period, which includes the majority of our new detections, our catalog may contain important information on the mechanisms of aftershock propagation and its relation to afterslip at Parkfield (e.g., Jiang *et al.*, 2021). From our initial observations, in the aftershock period, we can identify the logarithmic-time expansion of the aftershocks in the weeks following the mainshock that extends to about 38 km northwest along-strike into the creeping section. The PKD-MR catalog also has the potential to be used for further studies on external stress interactions with the Parkfield section and the 2004 sequence, for example, tidal stress modulations (e.g., Delorey *et al.*, 2017) or dynamic stresses imposed by distant earthquakes such as the 2004 M_w 9.1 Sumatra earthquake (e.g., Taira *et al.*, 2009).

Data and Resources

The Parkfield matched filter relocated (PKD-MR) earthquake catalog is provided as part of the supplemental material. We also include our local detections and template catalogs to allow easy reproduction. Differential travel-time measurements can be shared upon request. Seismic waveforms used for detection and relocation can be downloaded from the Northern California Earthquake Data Center (NCEDC) and Southern California Earthquake Data Center (SCEDC) data centers. Waveforms were retrieved using ObsPy (Beyreuther *et al.*, 2010) for networks BP (Northern California Earthquake Data Center [NCEDC], 2014), NC (USGS Menlo Park, 1967), CI (California Institute of Technology and United States Geological Survey Pasadena, 1926), and PG (Central Coast Seismic Network, PG&E). The supplemental material includes additional figures, the velocity model used for relocation, and descriptions of the supplementary catalogs.

Declaration of Competing Interests

The authors acknowledge that there are no conflicts of interest recorded.

Acknowledgments

This project is supported by National Science Foundation Earthscope program Grants EAR-1736197 (Z. P. and M. N.) and EAR-1736078 (G. L.). M. N. is supported by a Ph.D. fellowship from the Portuguese research foundation Fundação para a Ciência e Tecnologia (FCT), Grant SFRH/BD/139033/2018. Figures were generated using Generic Mapping Tools (Wessel *et al.*, 2019) and Matploltib (Hunter, 2007). The authors thank Rob Skoumal, one anonymous reviewer, and the Data Mine editor Taka'aki Taira for constructive comments and reviews. The authors also thank Roland Bürgmann for providing feedback.

References

Abercrombie, R. E. (1996). The magnitude-frequency distribution of earthquakes recorded with deep seismometers at Cajon Pass, southern California, *Tectonophysics* **261,** no. 1, 1–7, doi: 10.1016/0040-1951(96)00052-2.

Allen, R. V. (1978). Automatic earthquake recognition and timing from single traces, *Bull. Seismol. Soc. Am.* **68,** 1521–1532, doi: 10.1353/cch.2001.0013.

Amitrano, D. (2003). Brittle-ductile transition and associated seismicity: Experimental and numerical studies and relationship with the *b* value, *J. Geophys. Res.* **108,** no. B1, doi: 10.1029/2001jb000680.

Aron, A., and J. L. Hardebeck (2009). Seismicity rate changes along the central California coast due to stress changes from the 2003 M 6.5 San Simeon and 2004 M 6.0 Parkfield earthquakes, *Bull. Seismol. Soc. Am.* **99,** no. 4, 2280–2292, doi: 10.1785/0120080239.

Bakun, W. H., and A. G. Lindh (1985). The Parkfield, California, earthquake prediction experiment, *Science* **229,** no. 4714, 619–624, doi: 10.1126/science.229.4714.619.

Bakun, W. H., B. Aagaard, B. Dost, W. L. Ellsworth, J. L. Hardebeck, R. A. Harris, C. Ji, M. J. S. Johnston, J. Langbein, J. J. Lienkaemper, *et al.* (2005). Implications for prediction and hazard assessment from the 2004 Parkfield earthquake, *Nature* **437,** 969–974, doi: 10.1038/nature04067.

Barbot, S., Y. Fialko, and Y. Bock (2009). Postseismic deformation due to the M w 6.0 2004 Parkfield earthquake: Stress-driven creep on a fault with spatially variable rate-and-state friction parameters, *J. Geophys. Res.* **114,** no. B7, doi: 10.1029/2008JB005748.

Ben-Zion, Y., and I. Zaliapin (2020). Localization and coalescence of seismicity before large earthquakes, *Geophys. J. Int.* **223,** no. 1, 561–583, doi: 10.1093/gji/ggaa315.

Beyreuther, M., R. Barsch, L. Krischer, T. Megies, Y. Behr, and J. Wassermann (2010). ObsPy: A python toolbox for seismology, *Seismol. Res. Lett.* **81,** no. 3, 530–533, doi: 10.1785/gssrl.81.3.530.

Borcherdt, R. D., M. J. S. Johnston, G. Glassmoyer, and C. Dietel (2006). Recordings of the 2004 Parkfield earthquake on the general earthquake observation system array: Implications for earthquake precursors, fault rupture, and coseismic strain changes, *Bull. Seismol. Soc. Am.* **96,** no. 4B, S73–S89, doi: 10.1785/0120050827.

Brenguier, F., N. M. Shapiro, M. Campillo, V. Ferrazzini, Z. Duputel, O. Coutant, and A. Nercessian (2008). Towards forecasting volcanic eruptions using seismic noise, *Nat. Geosci.* **1,** no. 2, 126–130, doi: 10.1038/ngeo104.

Cabrera, L., P. Poli, and W. B. Frank (2022). Tracking the spatio-temporal evolution of foreshocks preceding the Mw 6.1 2009 L'Aquila earthquake, *J. Geophys. Res.* **127,** no. 3, e2021JB023888 , doi: 10.1029/2021JB023888.

California Institute of Technology and United States Geological Survey Pasadena (1926). Southern California Seismic Network, *International Federation of Digital Seismograph Networks*, doi: 10.7914/SN/CI.

Chun, K.-Y., Q.-Y. Yuan, and G. A. Henderson (2010). Precursory rise of P-wave attenuation before the 2004 Parkfield earthquake, *Bull. Seismol. Soc. Am.* **100,** 509–521, doi: 10.1785/0120090104.

Custódio, S., and R. J. Archuleta (2007). Parkfield earthquakes: Characteristic or complementary? *J. Geophys. Res.* **112,** no. B5, doi: 10.1029/2006JB004617.

Dascher-Cousineau, K., T. Lay, and E. E. Brodsky (2020). Two foreshock sequences post Gulia and Wiemer (2019), *Seismol. Res. Lett.* **91,** 2843–2850, doi: 10.1785/0220200082.

Delorey, A. A., N. J. van der Elst, and P. A. Johnson (2017). Tidal triggering of earthquakes suggests poroelastic behavior on the San Andreas fault, *Earth Planet. Sci. Lett.* **460,** 164–170, doi: 10.1016/j.epsl.2016.12.014.

Dieterich, J. H. (1978). Preseismic fault slip and earthquake prediction, *J. Geophys. Res.* **83,** no. B8, 3940–3948, doi: 10.1029/JB083iB08p03940.

Eberhart-Phillips, D., and A. J. Michael (1993). Three-dimensional velocity structure, seismicity, and fault structure in the Parkfield region, central California, *J. Geophys. Res.* **98,** no. B9, 15,737–15,758, doi: 10.1029/93JB01029.

Enescu, B., J. Mori, and M. Miyazawa (2007). Quantifying early aftershock activity of the 2004 mid-Niigata prefecture earthquake (M_w 6.6), *J. Geophys. Res.* **112,** no. B4, doi: 10.1029/2006JB004629.

Eshelby, J. D., and R. E. Peierls (1957). The determination of the elastic field of an ellipsoidal inclusion, and related problems, *Proc. Math. Phys. Eng. Sci.* **241,** 376–396, doi: 10.1098/rspa.1957.0133.

Ghosh, A., J. E. Vidale, Z. Peng, K. C. Creager, and H. Houston (2009). Complex nonvolcanic tremor near Parkfield, California, triggered by the great 2004 Sumatra earthquake, *J. Geophys. Res.* **114,** no. B12, doi: 10.1029/2008JB006062.

Gibbons, S. J., and F. Ringdal (2006). The detection of low magnitude seismic events using array-based waveform correlation, *Geophys. J. Int.* **165,** 149–166, doi: 10.1111/j.1365-246X.2006.02865.x.

Gulia, L., and S. Wiemer (2019). Real-time discrimination of earthquake foreshocks and aftershocks, *Nature* **574,** 193–199, doi: 10.1038/s41586-019-1606-4.

Gutenberg, B., and C. F. Richter (1944). Frequency of earthquakes in California, *Bull. Seismol. Soc. Am.* **34,** no. 4, 185–188, doi: 10.1785/bssa0340040185.

Herrmann, M., and W. Marzocchi (2021). Inconsistencies and lurking pitfalls in the magnitude–frequency distribution of high-resolution earthquake catalogs, *Seismol. Res. Lett.* **92,** no. 2A, 909–922, doi: 10.1785/0220200337.

Hunter, J. D. (2007). Matplotlib: A 2D graphics environment, *Comput. Sci. Eng.* **9,** no. 3, 90–95, doi: 10.1109/MCSE.2007.55.

Ishimoto, M., and K. Iida (1939). Observations of earthquakes registered with the microseismograph constructed recently, *Bull. Earthq. Res. Inst.* **17,** 443–478.

Jiang, J., Y. Bock, and E. Klein (2021). Coevolving early afterslip and aftershock signatures of a San Andreas fault rupture, *Sci. Adv.* **7,** no. 15, eabc1606, doi: 10.1126/sciadv.abc1606.

Johnston, M. J. S. (2006). Seismomagnetic effects from the long-awaited 28 September 2004 M 6.0 Parkfield earthquake, *Bull. Seismol. Soc. Am.* **96,** no. 4B, S206–S220, doi: 10.1785/0120050810.

Johnston, M. J. S., R. D. Borcherdt, A. T. Linde, and M. T. Gladwin (2006). Continuous borehole strain and pore pressure in the near field of the 28 September 2004 M 6.0 Parkfield, California, earthquake: Implications for nucleation, fault response, earthquake prediction, and tremor, *Bull. Seismol. Soc. Am.* **96,** no. 4B, S56–S72, doi: 10.1785/0120050822.

Kagan, Y. Y. (2004). Short-term properties of earthquake catalogs and models of earthquake source, *Bull. Seismol. Soc. Am.* **94,** no. 4, 1207–1228, doi: 10.1785/012003098.

Kato, N. (2007). Expansion of aftershock areas caused by propagating post-seismic sliding, *Geophys. J. Int.* **168,** no. 2, 797–808, doi: 10.1111/j.1365-246x.2006.03255.x.

Kato, A., and Y. Ben-Zion (2021). The generation of large earthquakes, *Nat. Rev. Earth Environ.* **2,** no. 1, 26–39, doi: 10.1038/s43017-020-00108-w.

Khoshmanesh, M., and M. Shirzaei (2018). Episodic creep events on the San Andreas fault caused by pore pressure variations, *Nat. Geosci.* **11,** no. 8, 610–614, doi: 10.1038/s41561-018-0160-2.

Langbein, J., R. Borcherdt, D. Dreger, J. Fletcher, J. L. Hardebeck, M. Hellweg, C. Ji, M. Johnston, J. R. Murray, R. Nadeau, *et al.* (2005). Preliminary report on the 28 September 2004, M 6.0 Parkfield, California earthquake, *Seismol. Res. Lett.* **76,** no. 1, 10–26, doi: 10.1785/gssrl.76.1.10.

Li, Z., and Z. Peng (2016). An automatic phase picker for local earthquakes with predetermined locations: Combining a signal-to-noise ratio detector with 1D velocity model inversion, *Seismol. Res. Lett.* **87,** no. 6, 1397–1405, doi: 10.1785/0220160027.

Lilliefors, H. W. (1969). On the Kolmogorov-Smirnov test for the exponential distribution with mean unknown, *J. Am. Stat. Assoc.* **64,** no. 325, 387–389, doi: 10.2307/2283748.

Lin, G. (2018). The source-specific station term and waveform cross-correlation earthquake location package and its applications to California and New Zealand, *Seismol. Res. Lett.* **89,** no. 5, 1877–1885, doi: 10.1785/0220180108.

Lin, G. (2020). Waveform cross-correlation relocation and focal mechanisms for the 2019 ridgecrest earthquake sequence, *Seismol. Res. Lett.* **91,** no. 4, 2055–2061, doi: 10.1785/0220190277.

Lin, G., Z. Peng, and M. Neves (2022). Comparisons of in situ Vp/Vs ratios and seismic characteristics between northern and southern California, *Geophys. J. Int.* **229,** no. 3, 2162–2174, doi: 10.1093/gji/ggac038.

Lomax, A., and A. Savvaidis (2022). High-precision earthquake location using source-specific station terms and inter-event waveform similarity, *J. Geophys. Res.* **127,** no. 1, e2021JB023190, doi: 10.1029/2021JB023190.

Marzocchi, W., I. Spassiani, A. Stallone, and M. Taroni (2019). How to be fooled searching for significant variations of the b-value, *Geophys. J. Int.* **220,** no. 3, 1845–1856, doi: 10.1093/gji/ggz541.

Matthews, M. V., and P. A. Reasenberg (1988). Statistical methods for investigating quiescence and other temporal seismicity patterns, *Pure Appl. Geophys.* **126,** nos. 2/4, 357–372, doi: 10.1007/bf00879003.

Meng, X., Z. Peng, and J. L. Hardebeck (2013). Seismicity around Parkfield correlates with static shear stress changes following the 2003 M_w 6.5 San Simeon earthquake, *J. Geophys. Res.* **118,** no. 7, 3576–3591, doi: 10.1002/jgrb.50271.

Michelini, A., and T. V. McEvilly (1991). Seismological studies at Parkfield. I. Simultaneous inversion for velocity structure and hypocenters using cubic B-splines parameterization, *Bull. Seismol. Soc. Am.* **81,** no. 2, 524–552, doi: 10.1785/BSSA0810020524.

Mignan, A. (2014). The debate on the prognostic value of earthquake foreshocks: A meta-analysis, *Sci. Rep.* **4,** no. 1, 4099, doi: 10.1038/srep04099.

Mogi, K. (1969). Some features of recent seismic activity in and near Japan (2), activity before and after great earthquakes, *Bull. Earthq. Res. Inst. Univ. Tokyo* **47,** 395–417.

Nadeau, R. M., and A. Guilhem (2009). Nonvolcanic tremor evolution and the San Simeon and Parkfield, California, earthquakes, *Science* **325,** 191–193, doi: 10.1126/science.1174155.

Nanjo, K. Z. (2020). Were changes in stress state responsible for the 2019 Ridgecrest, California, earthquakes? *Nat. Commun.* **11,** 3082, doi: 10.1038/s41467-020-16867-5.

Northern California Earthquake Data Center (NCEDC) (2014). High Resolution Seismic Network (HRSN), *Northern California Earthquake Data Center*, doi: 10.7932/HRSN.

Olson, E. L., and R. M. Allen (2005). The deterministic nature of earthquake rupture, *Nature* **438,** no. 7065, 212–215, doi: 10.1038/nature04214.

Oppenheimer, D. H., F. W. Klein, J. P. Eaton, and F. W. Lester (1993). The Northern California Seismic Network bulletin, January–December 1992, *Open-File Rept. 93–578*, doi: 10.3133/ofr93578.

Peng, Z., and P. Zhao (2009). Migration of early aftershocks following the 2004 Parkfield earthquake, *Nat. Geosci.* **2,** no. 12, 877–881, doi: 10.1038/ngeo697.

Peng, Z., J. E. Vidale, and H. Houston (2006). Anomalous early aftershock decay rate of the 2004 M_w 6.0 Parkfield, California, earthquake, *Geophys. Res. Lett.* **33,** L17307, doi: 10.1029/2006GL026744.

Perrin, C., F. Waldhauser, E. Choi, and C. H. Scholz (2019). Persistent fine-scale fault structure and rupture development: A new twist in the Parkfield, California, story, *Earth Planet. Sci. Lett.* **521,** 128–138, doi: 10.1016/j.epsl.2019.06.010.

Pritchard, M. E., R. M. Allen, T. W. Becker, M. D. Behn, E. E. Brodsky, R. Bürgmann, C. Ebinger, J. T. Freymueller, M. Gerstenberger, B. Haines, *et al.* (2020). New opportunities to study earthquake precursors, *Seismol. Res. Lett.* **91,** no. 5, 2444–2447, doi: 10.1785/0220200089.

Roeloffs, E. A. (2006). Evidence for aseismic deformation rate changes prior to earthquakes, *Annu. Rev. Earth Planet. Sci.* **34,** no. 1, 591–627, doi: 10.1146/annurev.earth.34.031405.124947.

Roeloffs, E., and J. Langbein (1994). The earthquake prediction experiment at Parkfield, California, *Rev. Geophys.* **32,** no. 3, 315, doi: 10.1029/94rg01114.

Ross, Z. E., D. T. Trugman, E. Hauksson, and P. M. Shearer (2019). Searching for hidden earthquakes in southern California, *Science* **364,** no. 6442, 767–771, doi: 10.1126/science.aaw6888.

Scholz, C. H. (2015). On the stress dependence of the earthquake b value, *Geophys. Res. Lett.* **42,** 1399–1402, doi: 10.1002/2014GL062863.

Schorlemmer, D., and S. Wiemer (2005). Microseismicity data forecast rupture area, *Nature* **434,** no. 7037, 1086–1086, doi: 10.1038/4341086a.

Schorlemmer, D., S. Wiemer, and M. Wyss (2004). Earthquake statistics at Parkfield: 1. Stationarity of b values, *J. Geophys. Res.* **109,** no. B12, doi: 10.1029/2004jb003234.

Shelly, D. R. (2009). Possible deep fault slip preceding the 2004 Parkfield earthquake, inferred from detailed observations of tectonic tremor, *Geophys. Res. Lett.* **36,** no. 17, doi: 10.1029/2009GL039589.

Shelly, D. R. (2017). A 15 year catalog of more than 1 million low-frequency earthquakes: Tracking tremor and slip along the deep San Andreas fault, *J. Geophys. Res.* **122,** no. 5, 3739–3753, doi: 10.1002/2017JB014047.

Shelly, D. R. (2020). A high-resolution seismic catalog for the initial 2019 Ridgecrest earthquake sequence: Foreshocks, aftershocks, and faulting complexity, *Seismol. Res. Lett.* **91,** no. 4, 1971–1978, doi: 10.1785/0220190309.

Shelly, D. R., and J. L. Hardebeck (2019). Illuminating faulting complexity of the 2017 yellowstone maple creek earthquake swarm, *Geophys. Res. Lett.* **46,** no. 5, 2544–2552, doi: 10.1029/2018gl081607.

Shelly, D. R., and K. M. Johnson (2011). Tremor reveals stress shadowing, deep postseismic creep, and depth-dependent slip recurrence on the lower-crustal San Andreas fault near Parkfield, *Geophys. Res. Lett.* **38,** no. 13, doi: 10.1029/2011GL047863.

Shelly, D. R., G. C. Beroza, and S. Ide (2007). Non-volcanic tremor and low-frequency earthquake swarms, *Nature* **446,** 305–307, doi: 10.1038/nature05666.

Shelly, D. R., W. L. Ellsworth, and D. P. Hill (2016). Fluid-faulting evolution in high definition: Connecting fault structure and frequency-magnitude variations during the 2014 Long Valley Caldera, California, earthquake swarm, *J. Geophys. Res.* **121,** no. 3, 1776–1795, doi: 10.1002/2015JB012719.

Shelly, D. R., S. C. Moran, and W. A. Thelen (2013). Evidence for fluid-triggered slip in the 2009 Mount Rainier, Washington earthquake swarm, *Geophys. Res. Lett.* **40,** 1506–1512, doi: 10.1002/grl.50354.

Shelly, D. R., Z. Peng, D. P. Hill, and C. Aiken (2011). Triggered creep as a possible mechanism for delayed dynamic triggering of tremor and earthquakes, *Nat. Geosci.* **4,** no. 6, 384–388, doi: 10.1038/ngeo1141.

Taira, T., P. G. Silver, F. Niu, and R. M. Nadeau (2009). Remote triggering of fault-strength changes on the San Andreas fault at Parkfield, *Nature* **461,** no. 7264, 636–639, doi: 10.1038/nature08395.

Thurber, C., H. Zhang, F. Waldhauser, J. Hardebeck, A. Michael, and D. Eberhart-Phillips (2006). Three-dimensional compressional wavespeed model, earthquake relocations, and focal mechanisms for the Parkfield, California, region, *Bull. Seismol. Soc. Am.* **96,** no. 4B, S38–S49, doi: 10.1785/0120050825.

Tormann, T., S. Wiemer, S. Metzger, A. Michael, and J. L. Hardebeck (2013). Size distribution of Parkfield's microearthquakes reflects changes in surface creep rate, *Geophys. J. Int.* **193,** no. 3, 1474–1478, doi: 10.1093/gji/ggt093.

USGS Menlo Park (1967). USGS Northern California Network, *International Federation of Digital Seismograph Networks*, doi: 10.7914/SN/NC.

van der Elst, N. J. (2021). B-positive: A robust estimator of aftershock magnitude distribution in transiently incomplete catalogs, *J. Geophys. Res.* **126,** no. 2, e2020JB021027, doi: 10.1029/2020JB021027.

Waldhauser, F. (2000). A double-difference earthquake location algorithm: Method and application to the northern Hayward fault, California, *Bull. Seismol. Soc. Am.* **90,** 1353–1368, doi: 10.1785/0120000006.

Waldhauser, F., and D. P. Schaff (2008). Large-scale relocation of two decades of northern California seismicity using cross-correlation and double-difference methods, *J. Geophys. Res.* **113,** doi: 10.1029/2007JB005479.

Waldhauser, F., W. L. Ellsworth, D. P. Schaff, and A. Cole (2004). Streaks, multiplets, and holes: High-resolution spatio-temporal behavior of Parkfield seismicity, *Geophys. Res. Lett.* **31,** no. 18, doi: 10.1029/2004GL020649.

Wessel, P., J. F. Luis, L. Uieda, R. Scharroo, F. Wobbe, W. H. F. Smith, and D. Tian (2019). The Generic Mapping Tools version 6, *Geochem. Geophys. Geosys.* **20,** no. 11, 5556–5564, doi: 10.1029/2019GC008515.

Wiemer, S., and M. Wyss (2000). Minimum magnitude of completeness in earthquake catalogs: Examples from Alaska, the western United States, and Japan, *Bull. Seismol. Soc. Am.* **90,** no. 4, 859–869, doi: 10.1785/0119990114.

Woessner, J., and S. Wiemer (2005). Assessing the quality of earthquake catalogues: Estimating the magnitude of completeness and its uncertainty, *Bull. Seismol. Soc. Am.* **95,** no. 2, 684–698, doi: 10.1785/0120040007.

Wyss, M., and R. E. Habermann (1988). Precursory seismic quiescence, *Pure Appl. Geophys.* **126,** no. 2, 319–332, doi: 10.1007/BF00879001.

Yang, H., L. Zhu, and R. Chu (2009). Fault-plane determination of the 18 April 2008 Mount Carmel, Illinois, earthquake by detecting and relocating aftershocks, *Bull. Seismol. Soc. Am.* **99,** no. 6, 3413–3420, doi: 10.1785/0120090038.

Yao, D., Y. Huang, and J. L. Fox (2021). New insights into the Lake Erie fault system from the 2019 M_L 4.0 Ohio earthquake sequence, *Seismol. Res. Lett.* **92,** no. 4, 2531–2539, doi: 10.1785/0220200335.

Zhai, Q., Z. Peng, L. Y. Chuang, Y.-M. Wu, Y.-J. Hsu, and S. Wdowinski (2021). Investigating the impacts of a wet typhoon on microseismicity: A case study of the 2009 Typhoon Morakot in taiwan based on a template matching catalog, *J. Geophys. Res.* **126,** no. 12, e2021JB023026 , doi: 10.1029/2021JB023026.

Zhao, P., Z. Peng, and K. G. Sabra (2010). Detecting remotely triggered temporal changes around the Parkfield section of the San Andreas fault, *Earthq. Sci.* **23,** no. 5, 497–509, doi: 10.1007/s11589-010-0748-0.

Manuscript received 24 June 2022
Published online 22 November 2022